CHEMISTRY OF MATERIALS

Article

pubs.acs.org/cm

Fast Li-Ion-Conducting Garnet-Related $Li_{7-3x}Fe_xLa_3Zr_2O_{12}$ with Uncommon $I\bar{4}3d$ Structure

Reinhard Wagner,*[,†] Günther J. Redhammer,[†] Daniel Rettenwander,[‡] Gerold Tippelt,[†] Andreas Welzl,[§] Stefanie Taibl,[§] Jürgen Fleig,[§] Alexandra Franz,[∥] Werner Lottermoser,[†] and Georg Amthauer[†]

[†]Department of Chemistry and Physics of Materials, University of Salzburg, Hellbrunnerstraße 34, 5020 Salzburg, Austria

[‡]Center for Materials Science and Engineering, Massachusetts Institute of Technology, 77 Massachusetts Avenue, Cambridge, Massachusetts 02139-4307, United States

[§]Institute of Chemical Technologies and Analytics, Vienna University of Technology, Getreidemarkt 9/164EC, 1060 Vienna, Austria

[∥]Department of Structure and Dynamics of Energy Materials, Helmholtz-Zentrum Berlin, Hahn-Meitner-Platz 1, 14109 Berlin, Germany

Supporting Information

ABSTRACT: Fast Li-ion-conducting Li oxide garnets receive a great deal of attention as they are suitable candidates for solid-state Li electrolytes. It was recently shown that Ga-stabilized $Li_7La_3Zr_2O_{12}$ crystallizes in the acentric cubic space group $I\bar{4}3d$. This structure can be derived by a symmetry reduction of the garnet-type $Ia\bar{3}d$ structure, which is the most commonly found space group of Li oxide garnets and garnets in general. In this study, single-crystal X-ray diffraction confirms the presence of space group $I\bar{4}3d$ also for $Li_{7-3x}Fe_xLa_3Zr_2O_{12}$. The crystal structure was characterized by X-ray powder diffraction, single-crystal X-ray diffraction, neutron powder diffraction, and Mößbauer spectroscopy. The crystal−chemical behavior of Fe^{3+} in $Li_7La_3Zr_2O_{12}$ is very similar to that of Ga^{3+}. The symmetry reduction seems to be initiated by the ordering of Fe^{3+} onto the tetrahedral Li1 (12*a*) site of space group $I\bar{4}3d$. Electrochemical impedance spectroscopy measurements showed a Li-ion bulk conductivity of up to 1.38×10^{-3} S cm^{-1} at room temperature, which is among the highest values reported for this group of materials.

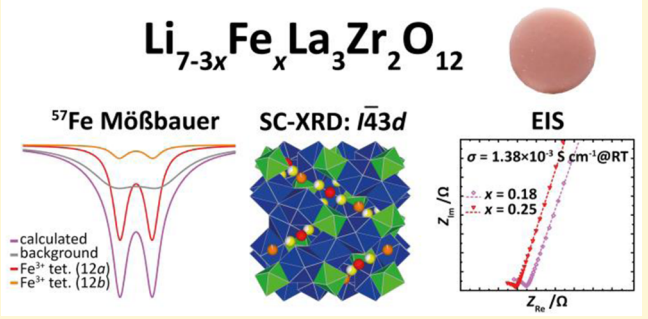

1. INTRODUCTION

The need for safe, powerful, and efficient energy storage devices has led to a high level of interest in the improvement of battery technologies. Currently, most commercially available Li-ion batteries contain organic polymer-based electrolytes, leading to multiple safety issues such as poor chemical and electrochemical stability, leakage, and flammability. These disadvantages have prevented this technology from reaching maturity. Therefore, next-generation Li-ion battery concepts are based on all-solid-state technologies using ceramic Li-ion conductors as electrolytes.[1−3] Li-stuffed oxide garnets containing more than three Li^+ ions per formula unit are among the most promising solid-state Li electrolytes. Cubic $Li_7La_3Zr_2O_{12}$ (LLZO) is considered as an especially suitable candidate. LLZO shows a high Li-ion conductivity as well as superior chemical and thermal stability. Its electrochemical inertness over a wide potential window and its stability against Li metal makes LLZO an especially promising material for use as a solid-state Li electrolyte.[1,4]

Pure LLZO occurs in two structural modifications. The tetragonal low-temperature phase in space group (SG) $I4_1/acd$ has a fully ordered Li^+ arrangement and shows a low ion conductivity of ~10^{-6} S cm^{-1} at room temperature (RT). The cubic high-temperature modification shows SG $Ia\bar{3}d$. The garnet-type $Ia\bar{3}d$ structure consists of a framework of 8-fold coordinated La^{3+} (24*c*) and octahedrally coordinated Zr^{4+} (16*a*). Li^+ occupies interstitial sites with tetrahedral (24*d*), octahedral (48*g*), and distorted 4-fold (96*h*) coordination. In contrast to the tetragonal modification, the cubic modification with SG $Ia\bar{3}d$ shows a disordered Li^+ distribution. The cubic modification can be stabilized at RT by the introduction of supervalent cations.[5−14] It was recently shown that the introduction of Ga^{3+} leads to a different structural modification with acentric cubic SG $I\bar{4}3d$ (Figure 1).[15,16] The formation of this SG is attributed to the site preference of Ga^{3+}, which causes a splitting of the 24*d* position of SG $Ia\bar{3}d$ into two different sites, namely, Li1 (12*a*) and Li2 (12*b*).

This study demonstrates that LLZO stabilized with Fe^{3+} also shows the acentric SG $I\bar{4}3d$. Coarse-grained samples of Fe-stabilized LLZO were prepared by solid-state reaction and

Received: June 21, 2016
Revised: July 25, 2016
Published: July 28, 2016

DOI: 10.1021/acs.chemmater.6b02516
Chem. Mater. 2016, 28, 5943−5951

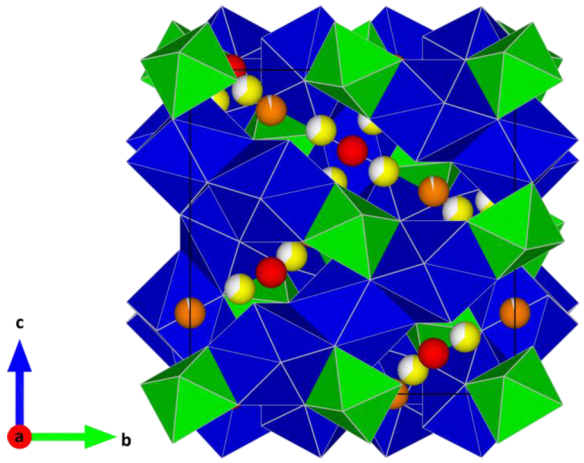

Figure 1. Crystal structure of LLZO with SG $I\bar{4}3d$. Blue dodecahedra represent 8-fold coordinated La^{3+} (Wyckoff position 24*d*) and green octahedra 6-fold coordinated Zr^{4+} (16*c*). Red spheres correspond to tetrahedrally coordinated Li^+ ions at the Li1 (12*a*) site; orange spheres represent tetrahedrally coordinated Li^+ ions at the Li2 (12*b*) site, and yellow spheres represent distorted 6-fold coordinated Li^+ ions at the Li3 (48*e*) site.

characterized by scanning electron microscopy (SEM)/back-scattered electron imaging (BSE) and energy-dispersive X-ray spectroscopy. The structural characterization was achieved by a rich portfolio of techniques, including X-ray powder diffraction (XRPD), single-crystal X-ray diffraction (SC-XRD), neutron powder diffraction (NPD), and ^{57}Fe Mößbauer spectroscopy. Electrochemical impedance spectroscopy (EIS) of Fe-stabilized LLZO reports a Li-ion bulk conductivity of up to 1.38×10^{-3} S cm^{-1} at RT, which is among the highest values reported for this group of materials.

2. EXPERIMENTAL SECTION

Synthesis. A series of $Li_{7-3x}Fe_xLa_3Zr_2O_{12}$ compounds with intended Fe concentrations (x) of 0.10, 0.16, 0.18, 0.20, 0.25, and 0.30 atoms per formula unit (pfu) were prepared by high-temperature sintering in air. The preparation route is equivalent to the procedure described by Wagner et al.[15] Li_2CO_3 (99%, Merck), Fe_2O_3 (99.945%, Alfa Aesar), La_2O_3 (99.99%, Alfa Aesar), and ZrO_2 (99.0%, Roth) were used as reagents. For the preparation of samples for ^{57}Fe Mößbauer spectroscopy, 15% of the intended Fe content was added as ^{57}Fe-enriched Fe_2O_3 (Isoflex, 95.47% enriched) and 85% as conventional Fe_2O_3 containing the natural mixture of isotopes. The starting materials were weighed out in their intended stoichiometric proportions with an excess of 10 wt % Li_2CO_3 to compensate for the loss of Li_2O due to evaporation during sintering. The reagents were mixed and ground in an agate mortar and then cold-pressed into pellets. The sample pellets were placed on a pellet of pure LLZO and then put into an alumina crucible. After being heated at a rate of 5 °C min^{-1} to 850 °C and sintered for 4 h, the pellets were ground in an agate mortar and ball-milled under isopropyl alcohol for 1 h (FRITSCH Pulverisette 7, 800 rpm, 2 mm ZrO_2 balls). The resulting powder was pressed into pellets and put into an alumina crucible. To avoid the incorporation of Al^{3+} from the crucible, the sample pellet was again placed on a pellet of pure LLZO. To reduce the Li_2O loss of the samples, the sample pellet was covered with another pellet of pure LLZO. The samples were heated at a rate of 5 °C min^{-1} to 1230 °C and sintered for 6 h.

SEM/EDX. SEM investigations were performed with a Zeiss Ultra Plus device to study the grain size, morphology, phase composition, and chemical homogeneity, i.e., the distribution of Fe, La, and Zr, by using BSE imaging mode and standard-free EDX measurements with an acceleration voltage of 20 kV. Special regard was given to the detection of Al and Ga, as well. For SEM characterization, polycrystalline chips from the pellets were embedded in an epoxy holder, polished with diamond paste, and coated with carbon.

XRPD. For the preparation of XRPD samples, small fragments from the sintered pellets were ground in an agate mortar. XPRD measurements were taken with a Bruker D8 Advance DaVinci Design diffractometer with a Lynxeye solid-state detector using Cu Kα radiation. Data were collected at 2θ positions between 10° and 80°. Evaluation of XRPD data was performed by Rietveld refinement using Bruker DIFFRACplus TOPAS (version 4.2).

SC-XRD. SC-XRD measurements were performed on a Bruker SMART APEX CCD diffractometer. Single crystals from gently crushed pellets were selected under the binocular on the basis of their optical properties. Selected crystals were glued on top of glass capillaries and tested on the diffractometer. To obtain good statistics, full sets of intensity data were collected on several crystals for each sample composition, resulting in a total of 18 data sets. In general, all tested crystals were of high quality and showed sharp reflections. Graphite-monochromatized Mo Kα radiation was used for data collection. The crystal-to-detector distance was 30 mm. The detector was positioned at 2θ positions of −30° and −50° using an ω-scan mode strategy at four different φ positions (0°, 90°, 180°, and 270°) for each 2θ position. For each run, 630 frames with $\Delta\omega$ = 0.3° were collected, so data were acquired in a large Q range up to minimum d values of ≈0.53 Å to obtain accurate anisotropic displacement parameters and to reduce the correlation between atomic displacement parameters and site occupation numbers. Three-dimensional data were integrated and corrected for Lorentz, polarization, and background effects by using the APEX2 software.[17] Structure solution with direct methods and subsequent weighted full-matrix least-squares refinements on F^2 were performed with SHELX-2012 as implemented in the program suite WinGX 2014.1.[18,19] Further structural analysis and visualizations of the crystal structure were performed by using the VESTA 3 program.[20]

NPD. Neutron powder diffraction data for samples with x = 0.18 pfu and x = 0.25 pfu were collected at the Research Reactor BER II at the Helmholtz-Zentrum Berlin. Both samples were stored under Ar directly after the synthesis to prevent the incorporation of H^+ and other reactions with H_2O and CO_2 from air. Powder diffraction data were acquired at 1.8 and 298 K in constant wavelength mode using the fine-resolution powder diffractometer FIREPOD with λ = 1.7982(1) Å.[21] Data were treated with the FULLPROF suite of programs.[22]

^{57}Fe Mößbauer Spectroscopy. The experimental spectra were recorded using the standard setup of the Mößbauer lab at the University of Salzburg. A ^{57}Co/Rh single-line thin source (initial activity of 50 mCi) was used to collect ^{57}Fe Mößbauer spectra of ^{57}Fe-enriched samples with x = 0.18 pfu and x = 0.25 pfu. Transmission powder spectra were recorded at RT with a multichannel analyzer (1024 channels) operating in conjunction with an electromechanical drive system with a symmetrical sawtooth velocity shape. For each composition, 50 mg of powdered sample was placed between plastic discs fitted into a Cu ring with a 10 mm inner diameter covered with Al foil on one side. The two simultaneously obtained spectra (512 channels each) were folded, calibrated against α-iron, and evaluated using RECOIL.[23]

EIS. The ionic conductivity was measured by electrochemical impedance spectroscopy (EIS). Thin films of platinum (200 nm) and titanium (10 nm) were sputtered on the top and bottom sides of the sample and act as ionically blocking electrodes. Titanium is needed to improve the adhesion of the platinum layer. For the EIS measurements, a Novocontrol Alpha analyzer was used in the frequency range of 3×10^6 to 10 Hz. Cooling and heating of the sample were performed with a Julabo F-25 HE instrument, which is a thermal bath fluid-based cooling and heating device. The temperature, measured by a thermocouple at the sample, was in the range of −7 to 25 °C.

3. RESULTS

Microstructure. For all compositions, coarse-grained samples with grain sizes of >100 μm were obtained. Individual

DOI: 10.1021/acs.chemmater.6b02516
Chem. Mater. 2016, 28, 5943−5951

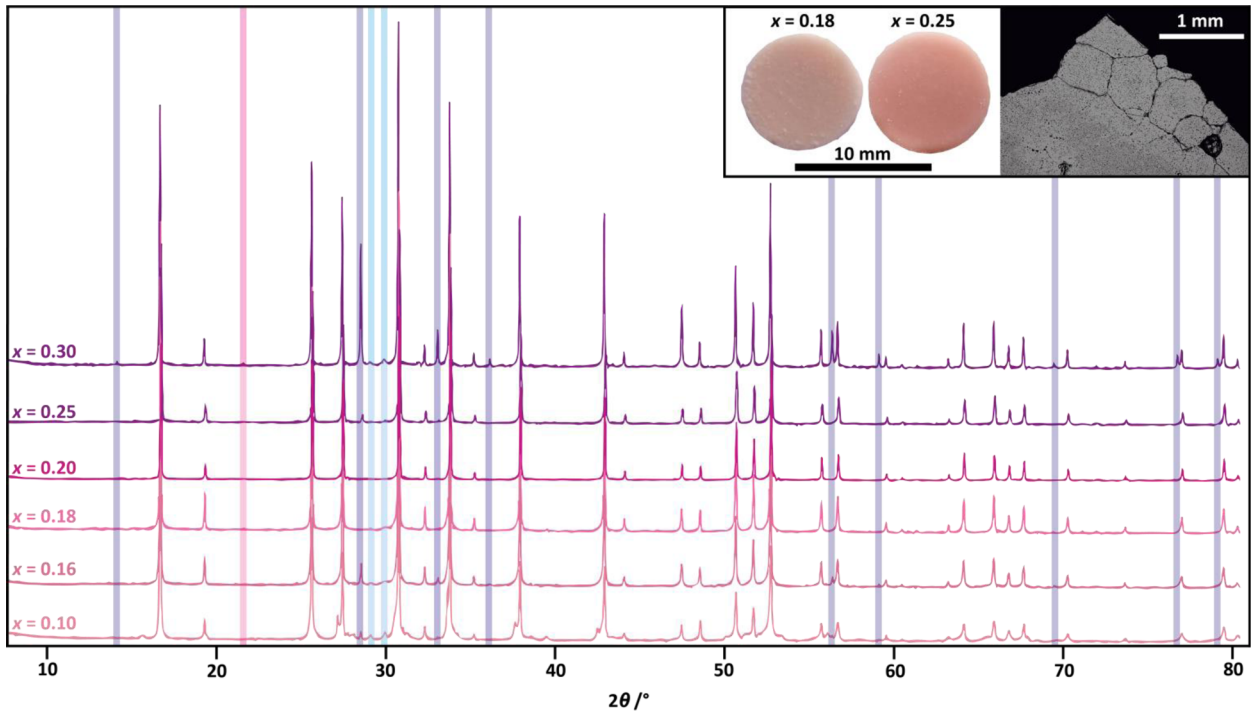

Figure 2. Comparison of XRPD patterns of $Li_{7-3x}Fe_xLa_3Zr_2O_{12}$ with x = 0.10 (bottom pattern), 0.16, 0.18, 0.20, 0.25, and 0.30 (top pattern). Reflections originating from extra phases are marked with violet ($La_2Zr_2O_7$) and blue (La_2O_3) bars; the characteristic reflection for SG $I\bar{4}3d$ at 2θ = 21.65° is marked with a red bar. The inset shows pictures of two sintered pellets with different Fe contents as well as a SEM-BSE image of a polished fragment of the x = 0.25 sample.

Table 1. Results of Rietveld Refinement of SC-XRD Data for Sample Fe30_2 [x_{Fe_ref} = 0.203; SG $I\bar{4}3d$; a_0 = 12.97670(10) Å]

atom	site	x	y	z	occupation	U_{eq}
La1	24*d*	0.11983(2)	0	1/4	0.4924(13)	0.00606(6)
Zr1	16*c*	−0.00022(2)	−0.00022(2)	−0.00022(2)	1.0	0.0047(1)
O1	48*e*	0.09754(18)	0.19627(18)	0.27948(18)	1.0	0.0083(4)
O2	48*e*	0.03366(2)	0.4453(2)	0.14704(18)	1.0	0.01039(4)
Li1	12*a*	3/8	0	1/4	0.1566(8)	0.0034(8)
Fe1					0.0309(8)	
Li2	12*b*	7/8	0	1/4	0.1846(8)	0.016(3)
Fe2					0.0029(8)	
Li3	48*e*	0.0972(8)	0.1864(8)	0.4276(8)	0.589(8)	0.0112(18)

grains show isometric shapes. Single grains separated by gaps are mainly found in the peripheral part of the pellets. In contrast to this, grains in the central part of the pellets do not show pronounced grain boundaries. Open voids are found as inclusions within single LLZO grains (see Figure S1). In some cases, extra phases are present along grain boundaries. SEM-BSE investigations did not show a zoning of LLZO grains.

Chemical Composition As Observed by SEM-EDX. EDX measurements of LLZO grains show the presence of La, Zr, and Fe. For all samples, the La/Zr ratio is <3/2, which indicates a deficiency of La relative to Zr on the order of a few percent compared to the intended overall La content. Fe contents of individual LLZO grains within one and the same pellet vary slightly. The average Fe content of the LLZO grains is slightly lower than the intended Fe content. In some cases, an extra phase containing La, Fe, and O with La > Fe was observed along grain boundaries. EDX mapping did not show a zoning of LLZO grains with regard to La, Zr, and Fe. No evidence of contamination with Al or Ga was indicated by EDX.

XRPD. The XRPD patterns of $Li_{7-3x}Fe_xLa_3Zr_2O_{12}$ with intended Fe concentrations of x = 0.10, 0.16, 0.18, 0.20, 0.25, and 0.30 pfu are shown in Figure 2. All samples show reflections matching the patterns observed for cubic LLZO; however, a definite distinction between the two cubic LLZO modifications with SG $I\bar{4}3d$ and $Ia\bar{3}d$ cannot be determined by XRPD. Only for the highly substituted sample with x = 0.30 is the characteristic 310 reflection for SG $I\bar{4}3d$ at 2θ = 21.65° (d = 4.10 Å) observed. For some samples, $La_2Zr_2O_7$ and La_2O_3 are observed as extra phases resulting from the loss of Li during sintering. The sample with the lowest intended Fe content of 0.10 pfu still shows 23 wt % tetragonal LLZO.

Crystal Structure According to SC-XRD. Single-crystal X-ray intensity data processing gives strong evidence of the cubic crystal system for all 18 data sets collected. For samples with a refined Fe content of x > 0.09, the analysis of intensity statistics and systematic extinctions yields the acentric SG $I\bar{4}3d$ (No. 220). Therefore, for the garnet family, atypical SG $I\bar{4}3d$ is found not only within the LLZO:Ga series, as described in great detail very recently by Wagner et al.,[15] but also for the incorporation of Fe^{3+} into the LLZO structure.[15] For more details about differences between common $Ia\bar{3}d$ and the acentric $I\bar{4}3d$ structure, the reader is referred to ref 15. Only for samples with

DOI: 10.1021/acs.chemmater.6b02516
Chem. Mater. 2016, 28, 5943−5951

a refined Fe content of $x < 0.09$ is the common LLZO SG $Ia\bar{3}d$ observed. This is in accordance with the LLZO:Ga series, where for small Ga^{3+} substitutions SG $Ia\bar{3}d$ is observed. Higher degrees of substitution force a reduction in symmetry due to ordering of Ga^{3+} onto one of the two possible tetrahedral sites. For structural refinement, the models of Wagner et al.[15] for $Ia\bar{3}d$ and $I\bar{4}3d$ structures were used as starting points.[15] In the final structural models, all atoms could be treated with anisotropic atomic displacement parameters and data sets could be refined for all data to wR_2 values of <6%.

Experimental data and results of structural refinement for selected samples are reported in Table S1; the fractional atomic coordinates, occupation numbers, and equivalent isotropic atomic displacement parameters are listed in Table 1 and Table S2, while selected bond lengths and angles are compiled in Table S3.

To summarize in brief, the crystal structure of Fe^{3+}-substituted LLZO, SG $I\bar{4}3d$, exhibits seven different atomic positions: La^{3+} occupies the 8-fold coordinated 24*d* position (site symmetry 2..), and Zr^{4+} is located at the octahedrally coordinated 16*c* position (site symmetry .3.). These positions are similar to those of the $Ia\bar{3}d$ structure. Li^+ is found at three different positions in $I\bar{4}3d$. Two of them correspond to the regular tetrahedral coordinated site of the silicate garnets (24*d* in $Ia\bar{3}d$); however, they split into two positions, namely, Li1 (12*a*) and Li2 (12*b*), both with site symmetry $\bar{4}$.., but they differ in bond lengths and polyhedral distortion. The third one is found at general position 48*e*, with site symmetry 1. This latter position is only partly occupied as is also common in LLZO compounds. Different from common silicate garnets, the acentric structure exhibits two independent oxygen atom positions, both in general position 48*e*. A graphical representation of the crystal structure of LLZO with SG $I\bar{4}3d$ is given in Figure 1.

For the $Ia\bar{3}d$ and $I\bar{4}3d$ structure, site occupation refinements yield a small deficit of La^{3+}; thus, the site occupation factor was allowed to vary freely during the refinements. The finding of a small La^{3+} deficit is consistent with results from EDX analysis and also was reported for LLZO:Ga. The number of La^{3+} vacancies varies within the $I\bar{4}3d$ structure from 0.12(2) pfu in Fe^{3+}-poor samples to 0.04(2) pfu in Fe^{3+}-rich samples, and there is some good evidence that the number of vacancies steadily decreases with an increase in Fe^{3+} content (Figure 3). Interestingly the two data points for the $Ia\bar{3}d$ structure are off of the trend and show a smaller La^{3+} deficit.

During refinement, the occupation factor of the octahedral 16*c* site, hosting Zr^{4+}, was allowed to refine freely. For samples with low Fe^{3+} concentrations in the $I\bar{4}3d$ structure, the results show a very small number of Zr^{4+} vacancies of <0.04 pfu on the 16*c* site when considering only Zr^{4+}. This might be overcome by placing Fe^{3+} at this site and assuming full occupancy. However, there is strong evidence from NPD data that the octahedral site is occupied by Zr^{4+} only. Also, in Mössbauer spectra, no evidence of octahedral Fe^{3+} was found.

For the $Ia\bar{3}d$ structure, strong evidence has shown that Fe^{3+} exclusively substitutes onto the tetrahedrally coordinated 24*d* position. To develop a site occupation model for the $I\bar{4}3d$ structure, a multiple-step process was used, which is described in detail in the Supporting Information and in Figure S2. It turned out that Fe^{3+} distinctly prefers the Li1 (12*a*) site, and only for higher overall Fe^{3+} concentrations are small amounts of ferric iron present at the Li2 (12*b*) site (Figure 3). This observation is fully in agreement with the results of Mößbauer

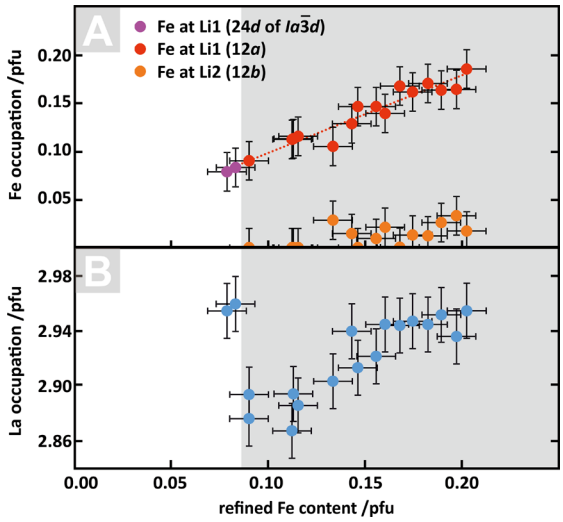

Figure 3. (A) Fe distribution over different Li sites as a function of the refined Fe content. (B) Occupation of the La site as a function of the refined Fe content.

spectroscopy, where indications of a second Fe^{3+} tetrahedral doublet with low intensity were found. Generally, both sites Li1 (12*a*) and Li2 (12*b*) show some vacancy concentrations, which were estimated to be 30% for Fe^{3+} concentrations of <0.15 pfu and decrease somewhat to 25% with an increasing overall Fe^{3+} content. The distinct preference of certain trivalent substituents for the Li1 (12*a*) site was already observed for LLZO:Ga. Again, it is assumed that the strong preference of Fe^{3+} for the Li1 (12*a*) site causes the reduction in symmetry from $Ia\bar{3}d$ to $I\bar{4}3d$.

For low overall Fe^{3+} concentrations, a large number of vacancies is observed at the Li2 (12*b*) site. The electron density progressively increases at the Li2 (12*b*) site with an increase in *x*, most probably because of an increasing amount of Li^+ present at this site. This is different from the case for the LLZO:Ga series, where higher occupations were found also for low Ga^{3+} concentrations. For higher Fe^{3+} concentrations, the Li^+ content of the Li2 (12*b*) site reaches a saturation level at 1.1 pfu of Li^+, assuming an additional electron density contribution from small amounts of Fe^{3+} at this site.

The occupation of the Li3 (48*e*) site generally was refined freely and gives a partial occupation of this site with Li^+. Even if the data show distinct scatter and the occupation number is highly correlated with the anisotropic displacement parameters, it is possible to deduce a decrease in the Li^+ occupation of the Li3 (48*e*) site with an increase in Fe^{3+} content at the Li1 (12*a*) site. The available data tentatively suggest that the substitution mechanism may follow the reaction $^{[48e]}Li_4 + {}^{[12a]}\square \rightarrow {}^{[48e]}Li_{4-3x} + {}^{[12a]}Fe_x$.

Analysis of equivalent isotropic atomic displacement parameters shows that Zr^{4+} generally has the smallest atomic displacement, followed by La^{3+}. Comparing the two oxygen ions, the atomic motion of the O2 position is larger than that of the O1 site. Different from the case for O1, the O^{2-} ion on the O2 site is bonded to the less localized Li2 (12*b*) site, which might result in greater motion. Generally, the atomic displacement parameters decrease with an increase in Fe^{3+} content, indicating that Fe^{3+} stabilizes the $I\bar{4}3d$ structure more and more. Li^+ ions show large atomic displacements with distinct anisotropic character of the displacement ellipsoids, especially at low substitutional levels at the Li2 (12*b*) site. With

DOI: 10.1021/acs.chemmater.6b02516
Chem. Mater. 2016, 28, 5943−5951

an increase in Fe^{3+} content, the equivalent isotropic atomic displacements decrease especially at the Li2 (12*b*) and Li3 (48*e*) sites, meaning the Li^+ ions on these sites become more precisely located (Figure S3).

Crystal Chemistry. The incorporation of Fe^{3+} into the structure of pure LLZO stabilizes the cubic structure. The lattice parameters thereby are reduced from 12.9831(4) to 12.9757(1) Å, and the decrease is almost linear (Figure 4). As

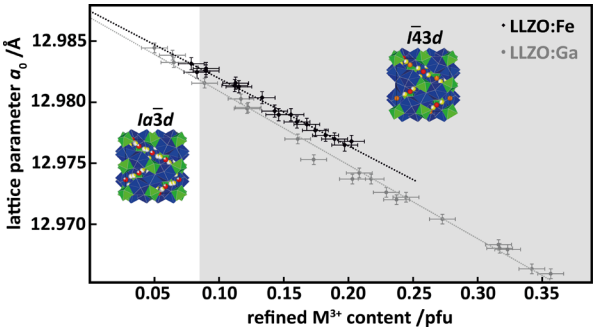

Figure 4. Lattice parameter a_0 of LLZO:Fe samples (black). For comparison, the data for LLZO:Ga from ref 15 are shown in gray.

for the LLZO:Ga series, there is no evident change in the slope when switching from $Ia\bar{3}d$ to $I\bar{4}3d$ symmetry. However, the slope of the data trend for the Fe^{3+} substitutional series is somewhat less steep than that for the LLZO:Ga series. For LLZO:Fe, a linear regression yields $a_0 = -0.0556x_{Fe} + 12.987$ (R^2 = 0.9876), i.e., a slope of −0.0556 Å x_{Fe}^{-1}, while for LLZO:Ga, the linear regression yields $a_0 = -0.0608x_{Ga} + 12.987$ (R^2 = 0.9929), i.e., a slope of −0.0608 Å x_{Ga}^{-1}. This trend is consistent with the ionic radii of tetrahedrally coordinated Fe^{3+} (0.49 Å) and Ga^{3+} (0.47 Å), replacing the larger Li^+ (0.59 Å).[24]

The variations of bond lengths and distortion parameters for the LLZO:Fe series follow closely the trends observed and described in detail for the LLZO:Ga series.[15] As for the LLZO:Ga series, the Li1 (12*a*) and Li2 (12*b*) tetrahedral sites in $I\bar{4}3d$ are different in bond length, tetrahedral distortion, and volume (Figures S4 and S5). The Li1 (12*a*) site shows smaller Li−O bond lengths and volumes; however, it displays distinct larger tetrahedral angle variance and quadratic tetrahedral elongation. It is worth noting that on the small substitutional level, the data points for both series plot well into the same trends. On the basis of site occupation refinements, the trivalent cations distinctly prefer the smaller tetrahedron. The distance between neighboring Li2 and Li3 decreases from 2.38 to ∼2.34 Å, while for the Li1−Li3 distance, this effect is not that clear (Figure S6). For the Li3 (48*e*) site, the average Li−O distance decreases with an increase in Fe^{3+} content and stabilizes at a value of ∼2.085 Å. The trends for the individual Li3−O bonds are diverse; some increase, and some decrease with an increase in trivalent cationic content. As shown in Figure S7, the overall polyhedral volume of the Li3 (48*e*) site (as LiO_6) decreases with an increase in M^{3+} (M = Ga or Fe) level, which may be seen in light of the decrease in Li content.

NPD. Refinement of NPD data was performed on the basis of the structural model derived from SC-XRD and yields a very good coincidence (see Figure S8A and Table S4). The preference of Fe^{3+} for the Li1 (12*a*) site is also indicated by the results of NPD data refinement. The comparison of NPD measurements of one and the same sample at different temperatures, 1.8 and 298 K, shows that the occupation of Li1 (12*a*) and Li2 (12*b*) is temperature-dependent. At very low temperatures, the Li2 (12*b*) site is almost fully occupied while the Li1 (12*a*) site shows very low occupation. At RT, the occupancy of the Li2 (12*b*) site is decreased whereas the Li1 (12*a*) site hosts more Li^+ than at 1.8 K. In addition to these observations, the residual nuclear density of the low-temperature measurement of the x = 0.25 sample suggests the presence of two additional Li^+ positions that were not observed by SC-XRD (see Figure S8B and Table S5). Results of crystal structure refinement at 298 and 1.8 K indicate a distinct distribution and movement of Li^+ even at low temperatures (see Figure S9). A detailed evaluation and interpretation of the NPD results is given in the Supporting Information.

Fe Distribution According to ^{57}Fe Mößbauer Spectroscopy. The results of ^{57}Fe Mößbauer spectroscopy are listed in Table 2 and shown in Figure 5. XRPD of ^{57}Fe-enriched LLZO:Fe samples with intended Fe contents of 0.18 and 0.25 pfu showed pure phase cubic LLZO. Mößbauer spectra of both samples are very similar to the LLZO:Fe spectra reported previously.[13,14] The high background is attributed to poorly crystalline Fe-bearing impurity phases that were also detected by SEM-EDX. A satisfying fit of the spectra is achieved by using tetrahedrally coordinated Fe^{3+} only. These results are in full agreement with the findings obtained from SC-XRD. Aside from a broad doublet used to model the background, both samples can be fitted by using two doublets showing an isomer shift $\delta \approx 0.20$ mm s^{-1} and a quadrupole splitting $\Delta E_Q \approx 0.8$–1.0 mm s^{-1}. For LLZO and other garnet-like materials, similar values have been interpreted as tetrahedrally coordinated Fe^{3+} on the 24*d* site.[13,14,25,26] Under consideration of the results of SC-XRD, the results of ^{57}Fe Mößbauer spectroscopy obtained by this study are interpreted as Fe^{3+} on the Li1 (12*a*) and Li2 (12*b*) sites of LLZO:Fe with SG $I\bar{4}3d$. As the quality of the obtained spectra is comparatively poor, the quantitative interpretation of the Mößbauer spectra must be treated with caution. However, the results indicate that Fe^{3+} is unequally distributed over these two tetrahedral sites, which coincides with the structural model derived from SC-XRD. It has to be emphasized that attempts to include octahedrally coordinated Fe^{3+} in the fit were not successful. Therefore, we conclude that no significant amounts of Fe^{3+} are located on octahedral sites. In contrast to other studies of LLZO:Fe, neither indications of strongly distorted tetrahedrally coordinated Fe^{3+} on the 48*e* site of SG $I\bar{4}3d$, equivalent to the 96*h* site of SG $Ia\bar{3}d$, nor magnetic subpatterns were observed in this study.[13,14]

Table 2. ^{57}Fe Mößbauer Hyperfine Fit Parameters for $Li_{7-3x}Fe_xLa_3Zr_2O_{12}$ (x = 0.18 and x = 0.25)

	doublet 1 (background)				doublet 2 (Fe^{3+}@12*a*)				doublet 3 (Fe^{3+}@12*b*)			
x (pfu)	δ (mm s^{-1})	ΔE_Q (mm s^{-1})	fwhm (mm s^{-1})	A (%)	δ (mm s^{-1})	ΔE_Q (mm s^{-1})	fwhm (mm s^{-1})	A (%)	δ (mm s^{-1})	ΔE_Q (mm s^{-1})	fwhm (mm s^{-1})	A (%)
0.18	0.26	0.03	2.54	67	0.20	1.08	0.37	27	0.28	0.78	0.27	6
0.25	0.23	1.39	0.92	53	0.20	0.98	0.26	41	0.20	1.02	0.30	6

DOI: 10.1021/acs.chemmater.6b02516
Chem. Mater. 2016, 28, 5943−5951

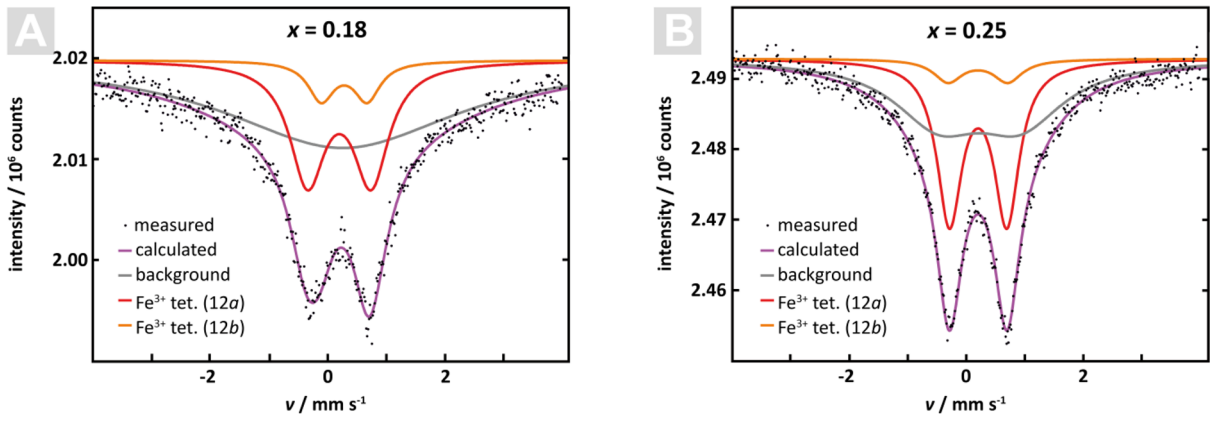

Figure 5. ^{57}Fe Mößbauer spectra of $Li_{7-3x}Fe_xLa_3Zr_2O_{12}$ with (A) $x = 0.18$ and (B) $x = 0.25$.

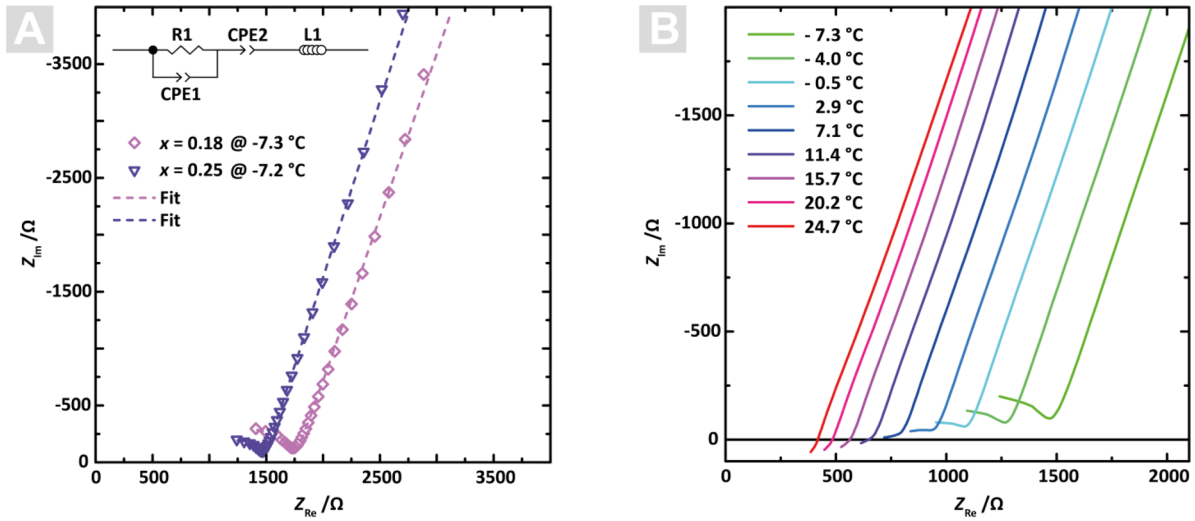

Figure 6. (A) Impedance spectra of LLZO:Fe measured at the lowest temperature (approximately −7 °C) with measurement data (symbols) and fits (dashed lines) according to the equivalent circuit shown in the graph. (B) Temperature-dependent impedance spectra of the $x = 0.25$ sample.

Li-Ion Conductivity As Seen by EIS. Impedance spectra of the Fe-stabilized LLZO garnets in Figure 6A display measurements at the lowest temperature (−7.3 °C). The spectra show parts of a high-frequency semicircle and a strong increase of the imaginary part toward lower frequencies. The latter can be attributed to the ionically blocking electrode. The high-frequency part can be described by a resistor (R_1) in parallel to a constant phase element (CPE1) with impedance

$$Z_{\mathrm{CPE1}} = \frac{1}{(i\omega)^n Q} \tag{1}$$

where ω is the angular frequency and Q and n are fit parameters. In series to R_1−CPE1, an inductance due to wiring is required for data analysis. In these spectra, there is no indication of interface or grain boundary effects, which would cause a second semicircle in the Nyquist plots.[12] When the blocking electrode is represented by another constant phase element, the circuit in Figure 6A results, which allows excellent fits of all data (see Figure 6A).

Resistance R_1 is interpreted in terms of a bulk transport process. A strong argument in favor of this assumption is the capacitance associated with the CPE according to[27]

$$C = (R^{1-n}Q)^{1/n} \tag{2}$$

On the basis of the obtained fit values for CPE1, the calculated capacitance is in the range of 10 pF. Using this value, sample area A, and thickness d, a relative permittivity can be calculated according to

$$\varepsilon_r = \frac{Cd}{A\varepsilon_0} \tag{3}$$

This leads to values on the order of 55−80, obtained for the measurements at the lowest temperature. These are realistic values for oxides and support the interpretation of the arc as a bulk property.[12] Therefore, resistance R_1 can be used to determine the Li-ion conduction in the bulk by

$$\sigma_{\mathrm{bulk}} = \frac{d}{R_1 A} \tag{4}$$

As can be seen in Figure 6B, the high-frequency semicircle in the impedance spectra vanishes upon heating of the sample to room temperature. The reason for this change is the increasing relaxation frequency of the LLZO bulk $\omega = 1/RC$ due to the temperature-dependent resistance. Nevertheless, the equivalent circuit in Figure 6A can also be applied for higher temperatures, and bulk resistances can be extracted for all temperatures.

The Arrhenius graph in Figure 7 shows that the activation energy is ∼0.29 eV for the samples. Very high ionic

DOI: 10.1021/acs.chemmater.6b02516
Chem. Mater. 2016, 28, 5943−5951

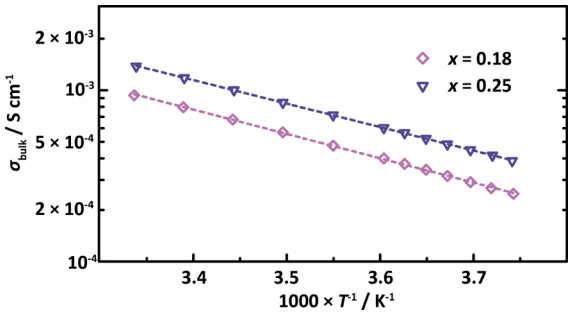

Figure 7. Temperature-dependent bulk conductivities for LLZO:Fe.

conductivities result at RT for the $x = 0.25$ pfu sample, reaching 1.38×10^{-3} S cm^{-1} at 23.5 °C (Table 3). This value is one of the highest bulk conductivities at RT measured for LLZO garnets so far ($\sigma = 1.3 \times 10^{-3}$ S cm^{-1} for $Li_{6.55}Ga_{0.15}La_3Zr_2O_{12}$, and $\sigma = 1.3 \times 10^{-3}$ S cm^{-1} for $Li_{6.4}La_3Zr_{1.4}Ta_{0.6}O_{12}$).[28,29]

Table 3. Li-Ion Conductivity σ_{bulk} and Activation Energy E_a at 23.5 °C for $Li_{7-3x}Fe_xLa_3Zr_2O_{12}$ ($x = 0.18$ and $x = 0.25$)

x (pfu)	σ_{bulk} (S cm^{-1})	E_a (eV)
0.18	9.35×10^{-4}	0.29
0.25	1.38×10^{-3}	0.28

4. DISCUSSION

It was shown that the substitution of Li^+ with ferric iron in LLZO induces a reduction in symmetry to SG $I\bar{4}3d$. Thereby, Fe^{3+} strongly prefers the Li1 (12*a*) site; this site preference is assumed to be a main reason for the change in symmetry. In light of recent observations for the LLZO:Ga and LLZO:(Al,Ga) series, the appearance of the $I\bar{4}3d$ symmetry also in the LLZO:Fe series might not be astonishing.[15,16] While the small Al^{3+} keeps $Ia\bar{3}d$ symmetry, the larger Ga^{3+} and even larger Fe^{3+} show the change in symmetry, indicating a strong influence of steric size effects on inducing the symmetry change. Indeed, Ga^{3+} and Fe^{3+} prefer the larger and more distorted Li1 (12*a*) tetrahedral site. One might speculate that a substitution with Sc^{3+} for Li^+ should be suitable for achieving $I\bar{4}3d$ symmetry for LLZO, as well; however, until now, Sc^{3+}-stabilized LLZO has not been synthesized successfully.

Even if refinement of Li site occupancies is delicate using X-ray diffraction, it could be shown, in analogy to the LLZO:Ga series, that the incorporation of Fe^{3+} scales with a reduction of the Li^+ content mainly at the Li3 (48*e*) interstitial site rather than with a reduction of the Li^+ content on the Li1 (12*a*) or Li2 (12*b*) tetrahedral site. This is in line with observations for SG $Ia\bar{3}d$.[29−31]

A phase transformation from SG $Ia\bar{3}d$ to SG $I\bar{4}3d$ caused by protonation as recently reported by several authors can be excluded for this study.[32−34] Samples were either immediately characterized after their synthesis or stored under Ar. Phase transformations due to protonation were reported either after a special treatment or after storage at RT for several years. In addition, a Li^+/H^+ exchange leads to an increase in lattice parameter a_0 to values of >13 Å. As the lattice parameter values reported in this study are in the range of 12.97 Å and thus well in accordance with those of other unaltered LLZO samples, we do not expect any significant protonation of the LLZO:Fe samples used in this study.

It is conspicuous that both members of the LLZO group with SG $I\bar{4}3d$ show superior ionic conductivity compared to that of the LLZO:Al group with SG $Ia\bar{3}d$, even if the differently stabilized samples were synthesized by the very same preparation route.[16] Rettenwander et al.[16] already discussed possible explanations for the improved ionic conductivity of LLZO:Ga compared to that of LLZO:Al. Besides other factors, they also supposed that the phase transformation from SG $Ia\bar{3}d$ to SG $I\bar{4}3d$ partially accounts for the enhanced electrochemical properties. The results of this study reinforce these assumptions, as the ionic conductivities of LLZO:Fe reported in this study are among the highest values reported for this class of materials. However, further electrochemical investigations will be needed to evaluate the aptitude of LLZO:Fe as a solid-state electrolyte, as the electrochemical stability of the transition element cation Fe^{3+} might be inferior compared to those of other stabilizing cations such as Al^{3+} and Ga^{3+}.

5. CONCLUSIONS

This study reveals that Fe-stabilized LLZO shows the acentric cubic SG $I\bar{4}3d$ (No. 220). This crystal structure was recently reported for Ga-stabilized LLZO and is different from those of other members of the Li oxide garnet group that show SG $Ia\bar{3}d$ (No. 230). Similar to that of Ga-stabilized LLZO, the phase transformation seems to be caused by the site preference of Fe^{3+}. Results of ^{57}Fe Mößbauer spectroscopy confirm the preference of Fe^{3+} for the tetrahedral Li1 (12*a*) site. Electrochemical impedance spectroscopy exhibits very high Li-ion bulk conductivity up to 1.38×10^{-3} S cm^{-1} at RT. These results confirm that garnet-similar LLZO materials with SG $I\bar{4}3d$ show superior Li-ion conductivity compared to that of conventional LLZO garnets with SG $Ia\bar{3}d$. Again, it must be highlighted that understanding the structure property relationship is essential for understanding the electrochemical properties of these electrolyte materials.

■ ASSOCIATED CONTENT

Supporting Information

The Supporting Information is available free of charge on the ACS Publications website at DOI: 10.1021/acs.chemmater.6b02516.

Distribution of open voids and sample morphology (Figure S1), results of electron density modeling for Li1 and Li2 sites of LLZO:Fe (Figure S2), variation of U_{iso} for different Li sites (Figure S3), variation of different Li−O bond lengths (Figure S4), TQE of different Li sites (Figure S5), variation of Li2−Li3 bond lengths (Figure S6), behavior of the LiO_6 polyhedral volume (Figure S7), refinement of NPD data using different structural models (Figure S8), residual nuclear density of LLZO:Fe at different temperatures (Figure S9), experimental setup and results of the crystal structure refinement of SC-XRD data (Table S1), atomic coordinates and atomic displacement parameters of selected LLZO:Fe samples (Table S2), selected bond lengths and distortion parameters (Table S3), results of Rietveld refinement of NPD data (Table S4), results of Rietveld refinement of NPD data using a structural model with five Li positions (Table S5), a detailed description of the development of a site occupation model for tetrahedral sites, and a detailed discussion of NPD results (PDF)

DOI: 10.1021/acs.chemmater.6b02516
Chem. Mater. 2016, 28, 5943−5951

X-ray crystallographic file CSD-431389 (Fe_1, SG $Ia\bar{3}d$) (CIF)
X-ray crystallographic file CSD-431390 (Fe10_5) (CIF)
X-ray crystallographic file CSD-431391 (Fe16_8) (CIF)
X-ray crystallographic file CSD-431392 (Fe25_2) (CIF)
X-ray crystallographic file CSD-431392 (Fe30_2) (CIF)

AUTHOR INFORMATION

Corresponding Author

*E-mail: reinhard.wagner@sbg.ac.at.

Notes

The authors declare no competing financial interest.

ACKNOWLEDGMENTS

R.W., D.R., and G.A. acknowledge Austrian Science Fund (FWF) Project P25702 for financial support. This research project has been supported by the European Commission under the 7th Framework Programme through the "Research Infrastructure" action of the "Capacities" Programme, NMI3-II Grant 283883. The authors thank Helmholtz-Zentrum Berlin for the allocation of neutron radiation beam time.

REFERENCES

(1) Thangadurai, V.; Narayanan, S.; Pinzaru, D. Garnet-type solid-state fast Li ion conductors for Li batteries: critical review. *Chem. Soc. Rev.* **2014**, *43*, 4714−4727.

(2) Thangadurai, V.; Pinzaru, D.; Narayanan, S.; Baral, A. K. Fast Solid-State Li Ion Conducting Garnet-Type Structure Metal Oxides for Energy Storage. *J. Phys. Chem. Lett.* **2015**, *6*, 292−299.

(3) Zeier, W. G. Structural limitations for optimizing garnet-type solid electrolytes: a perspective. *Dalton T* **2014**, *43*, 16133−16138.

(4) Cussen, E. J. Structure and ionic conductivity in lithium garnets. *J. Mater. Chem.* **2010**, *20*, 5167−5173.

(5) Buschmann, H.; Dolle, J.; Berendts, S.; Kuhn, A.; Bottke, P.; Wilkening, M.; Heitjans, P.; Senyshyn, A.; Ehrenberg, H.; Lotnyk, A.; Duppel, V.; Kienle, L.; Janek, J. Structure and dynamics of the fast lithium ion conductor "$Li_7La_3Zr_2O_{12}$". *Phys. Chem. Chem. Phys.* **2011**, *13*, 19378−19392.

(6) Geiger, C. A.; Alekseev, E.; Lazic, B.; Fisch, M.; Armbruster, T.; Langner, R.; Fechtelkord, M.; Kim, N.; Pettke, T.; Weppner, W. Crystal Chemistry and Stability of "$Li_7La_3Zr_2O_{12}$" Garnet: A Fast Lithium-Ion Conductor. *Inorg. Chem.* **2011**, *50*, 1089−1097.

(7) Rettenwander, D.; Geiger, C. A.; Tribus, M.; Tropper, P.; Amthauer, G. A Synthesis and Crystal Chemical Study of the Fast Ion Conductor $Li_{7-3x}Ga_xLa_3Zr_2O_{12}$ with x = 0.08 to 0.84. *Inorg. Chem.* **2014**, *53*, 6264−6269.

(8) Afyon, S.; Krumeich, F.; Rupp, J. L. M. A shortcut to garnet-type fast Li-ion conductors for all-solid state batteries. *J. Mater. Chem. A* **2015**, *3*, 18636−18648.

(9) Thompson, T.; Wolfenstine, J.; Allen, J. L.; Johannes, M.; Huq, A.; David, I. N.; Sakamoto, J. Tetragonal vs. cubic phase stability in Al - free Ta doped $Li_7La_3Zr_2O_{12}$ (LLZO). *J. Mater. Chem. A* **2014**, *2*, 13431−13436.

(10) Wang, D. W.; Zhong, G. M.; Dolotko, O.; Li, Y. X.; McDonald, M. J.; Mi, J. X.; Fu, R. Q.; Yang, Y. The synergistic effects of Al and Te on the structure and Li^+-mobility of garnet-type solid electrolytes. *J. Mater. Chem. A* **2014**, *2*, 20271−20279.

(11) Hubaud, A. A.; Schroeder, D. J.; Key, B.; Ingram, B. J.; Dogan, F.; Vaughey, J. T. Low temperature stabilization of cubic $(Li_{7-x}Al_{x/3})$-$La_3Zr_2O_{12}$: role of aluminum during formation. *J. Mater. Chem. A* **2013**, *1*, 8813.

(12) Rettenwander, D.; Welzl, A.; Cheng, L.; Fleig, J.; Musso, M.; Suard, E.; Doeff, M. M.; Redhammer, G. J.; Amthauer, G. Synthesis, Crystal Chemistry, and Electrochemical Properties of $Li_{7-2x}La_3Zr_{2-x}Mo_xO_{12}$ (x = 0.1−0.4): Stabilization of the Cubic Garnet Polymorph via Substitution of Zr^{4+} by Mo^{6+}. *Inorg. Chem.* **2015**, *54*, 10440−10449.

(13) Rettenwander, D.; Geiger, C. A.; Amthauer, G. Synthesis and Crystal Chemistry of the Fast Li-Ion Conductor $Li_7La_3Zr_2O_{12}$ Doped with Fe. *Inorg. Chem.* **2013**, *52*, 8005−8009.

(14) Rettenwander, D.; Geiger, C. A.; Tribus, M.; Tropper, P.; Wagner, R.; Tippelt, G.; Lottermoser, W.; Amthauer, G. The solubility and site preference of Fe^{3+} in $Li_{7-3x}Fe_xLa_3Zr_2O_{12}$ garnets. *J. Solid State Chem.* **2015**, *230*, 266−271.

(15) Wagner, R.; Redhammer, G. J.; Rettenwander, D.; Senyshyn, A.; Schmidt, W.; Wilkening, M.; Amthauer, G. Crystal Structure of Garnet-Related Li-Ion Conductor $Li_{7-3x}Ga_xLa_3Zr_2O_{12}$: Fast Li-Ion Conduction Caused by a Different Cubic Modification? *Chem. Mater.* **2016**, *28*, 1861−1871.

(16) Rettenwander, D.; Redhammer, G.; Preishuber-Pflügl, F.; Cheng, L.; Miara, L.; Wagner, R.; Welzl, A.; Suard, E.; Doeff, M. M.; Wilkening, M.; Fleig, J.; Amthauer, G. Structural and Electrochemical Consequences of Al and Ga Cosubstitution in $Li_7La_3Zr_2O_{12}$Solid Electrolytes. *Chem. Mater.* **2016**, *28*, 2384−2392.

(17) *APEX2*; Bruker AXS Inc.: Madison, WI, 2012.

(18) Farrugia, L. J. WinGX and ORTEP for Windows: an update. *J. Appl. Crystallogr.* **2012**, *45*, 849−854.

(19) Sheldrick, G. M. Crystal structure refinement with SHELXL. *Acta Crystallogr., Sect. C: Struct. Chem.* **2015**, *71*, 3−8.

(20) Momma, K.; Izumi, F. VESTA 3for three-dimensional visualization of crystal, volumetric and morphology data. *J. Appl. Crystallogr.* **2011**, *44*, 1272−1276.

(21) Többens, D. M.; Stüßer, N.; Knorr, K.; Mayer, H. M.; Lampert, G. E9: The New High-Resolution Neutron Powder Diffractometer at the Berlin Neutron Scattering Center. *Mater. Sci. Forum* **2001**, *378−381*, 288−293.

(22) Rodriguez-Carvajal, J. Magnetic structure determination from powder diffraction using the program FullProf. *Appl. Crystallogr.* **2000**, 30−36.

(23) Rancourt, D. G.; Lagarec, D. *Recoil User Manual: Mössbauer Spectral Analysis Software for Windows*; University of Ottawa: Ottawa, ON, 1998.

(24) Shannon, R. D. Revised Effective Ionic-Radii and Systematic Studies of Interatomic Distances in Halides and Chalcogenides. *Acta Crystallogr., Sect. A: Cryst. Phys., Diffr., Theor. Gen. Crystallogr.* **1976**, *32*, 751−767.

(25) Amthauer, G.; Annerste, H.; Hafner, S. S. The Mössbauer spectrum of ^{57}Fe in silicate garnets. *Z. Kristallogr. - Cryst. Mater.* **1976**, *143*, 14−55.

(26) Nitsche, R.; Tippelt, G.; Amthauer, G. Kinetics and thermodynamics of intracrystalline Fe-Ga distribution in $Y_3(Fe, Ga)_5O_{12}$. *J. Mater. Sci.* **1994**, *29*, 2903−2910.

(27) Fleig, J. The grain boundary impedance of random microstructures: numerical simulations and implications for the analysis of experimental data. *Solid State Ionics* **2002**, *150*, 181−193.

(28) Bernuy-Lopez, C.; Manalastas, W.; Lopez del Amo, J. M.; Aguadero, A.; Aguesse, F.; Kilner, J. A. Atmosphere Controlled Processing of Ga-Substituted Garnets for High Li-Ion Conductivity Ceramics. *Chem. Mater.* **2014**, *26*, 3610−3617.

(29) Li, Y. T.; Han, J. T.; Wang, C. A.; Xie, H.; Goodenough, J. B. Optimizing Li^+ conductivity in a garnet framework. *J. Mater. Chem.* **2012**, *22*, 15357−15361.

(30) Mukhopadhyay, S.; Thompson, T.; Sakamoto, J.; Huq, A.; Wolfenstine, J.; Allen, J. L.; Bernstein, N.; Stewart, D. A.; Johannes, M. D. Structure and Stoichiometry in Supervalent Doped $Li_7La_3Zr_2O_{12}$. *Chem. Mater.* **2015**, *27*, 3658−3665.

(31) O'Callaghan, M. P.; Cussen, E. J. Lithium dimer formation in the Li-conducting garnets $Li_{5+x}Ba_xLa_{3-x}Ta_2O_{12}$ ($0 < x \leq 1.6$). *Chem. Commun.* **2007**, 2048−2050.

(32) Orera, A.; Larraz, G.; Rodriguez-Velamazan, J. A.; Campo, J.; Sanjuan, M. L. Influence of Li^+ and H^+ Distribution on the Crystal Structure of $Li_{7-x}H_xLa_3Zr_2O_{12}$ ($0 \leq x \leq 5$) Garnets. *Inorg. Chem.* **2016**, *55*, 1324−1332.

DOI: 10.1021/acs.chemmater.6b02516
Chem. Mater. 2016, 28, 5943−5951

(33) Larraz, G.; Orera, A.; Sanz, J.; Sobrados, I.; Diez-Gómez, V.; Sanjuán, M. L. NMR study of Li distribution in $Li_{7-x}H_xLa_3Zr_2O_{12}$ garnets. *J. Mater. Chem. A* **2015**, *3*, 5683−5691.
(34) Galven, C.; Suard, E.; Mounier, D.; Crosnier-Lopez, M.-P.; Le Berre, F. Structural characterization of a new acentric protonated garnet: $Li_{6-x}H_xCaLa_2Nb_2O_{12}$. *J. Mater. Res.* **2013**, *28*, 2147−2153.

DOI: 10.1021/acs.chemmater.6b02516
Chem. Mater. 2016, 28, 5943−5951